Title

Elucidating the Role of Halides and Iron during Radiolysis-Driven Oxidative Etching of Gold Nanocrystals Using Liquid Cell Transmission Electron Microscopy and Pulse Radiolysis

Journal

Journal of the American Chemical Society, 143(30)

ISSN

0002-7863

Authors

Crook, Michelle F
Laube, Christian
Moreno-Hernandez, Ivan A
et al.

Publication Date

2021-08-04

DOI

10.1021/jacs.1c05099

Peer reviewed

Elucidating the role of halides and iron during radiolysis driven oxidative etching of gold nanocrystals using liquid cell TEM and pulse radiolysis

Michelle F. Crook,[†] Christian Laube,[†^] Ivan A. Moreno-Hernandez,[†] Axel Kahnt,[‡] Stefan Zahn,[‡] Justin C. Ondry,[†‖] Aijia Liu,[†] A. Paul Alivisatos.[*,†,¶,§,‖]

†Department of Chemistry and ¶Department of Materials Science and Engineering, University of California—Berkeley, Berkeley, California 94720, United States

§Materials Sciences Division, Lawrence Berkeley National Laboratory, Berkeley, California 94720, United States

‡ Leibniz Institute of Surface Engineering (IOM), Permoserstr. 15, D-04318 Leipzig, Germany

‖Kavli Energy NanoScience Institute, University of California-Berkeley and Lawrence Berkeley National Laboratory, Berkeley, California 94720, United States

ABSTRACT: Graphene liquid cell transmission electron microscopy has enabled the observation of a variety of nanoscale transformations. Yet understanding the chemistry of the liquid cell solution and its impact on the observed chemical transformation remains an important step towards translating insights from the liquid cell TEM to bench-top chemistry. Gold nanocrystal etching can be used as a model system to probe the reactivity of the solution. $FeCl_3$ has been widely used to promote Au oxidation in bulk and liquid cell TEM studies, but the roles of the halide and iron species have not been fully elucidated. In this work, we observed the etching trajectories of gold nanocrystals in different iron halide solutions. We observed an increase in gold nanocrystal etch rate in going from Cl^-- to Br^-- to I^--containing solutions. This is consistent with a mechanism in which the dominant role of the halide is as complexation agents for oxidized Au species. It also suggests that hydroxyl radical scavenging and formation of oxidizing $X_2^{\cdot-}$ radicals is not a dominant mechanism. Additionally, iron has empirically been determined to induce etching of gold nanocrystals in liquid cell transmission electron microscopy, but the mechanism through which this happens remains unclear. Pulse radiolysis was used to gain spectroscopic insight into the role of iron in liquid cell transmission electron microscopy. Ground state bleaching of the Fe(III) absorption band indicates that iron may react with the $Cl_2^{\cdot-}$ radicals to form an oxidized, long-lived transient species under irradiation. CASSCF calculations indicated that the aqueous $FeCl_3$ complex is oxidized to an Fe species with reduced electron density at an OH ligand, which may act as the oxidant in this system. Liquid cell transmission electron microscopy studies support that a long-lived species is involved in the oxidative etching mechanism. Together our data indicates that an oxidized iron species may be the active oxidant in the system, while halides can modulate the etch rate by tuning the reduction potential of gold nanocrystals.

INTRODUCTION

The morphology of gold nanocrystals (AuNCs) can be controlled with high precision with careful control of the synthetic environment. Minute changes in precursor concentration,[1–4] or ppm-level impurities[5,6] can drastically change, or completely inhibit nanocrystal formation. This sensitivity to the environment has been exploited to create a variety of different nanocrystal morphologies.[3,7–9] This literature forms a foundation enabling a reverse approach. In systems where the chemical environment is not well understood or is challenging to probe, the evolution of pre-synthesized gold nanocrystals can be used as a tool to deduce the reactive species in the chemical environment.

One environmental system that has remained challenging to probe is the solution in liquid cell transmission electron microscopy (LCTEM). LCTEM is a technique where a solution is hermetically sealed between two electron transparent SiN membranes,[10] two graphene

coated TEM grids,[11] or amorphous carbon windows,[12] enabling *in situ* imaging of nanocrystal transformations in solution. LCTEM has led to discoveries of new methods of crystal growth,[10,11] kinetic intermediates of gold nanocrystals,[13–15] as well as the precise atomic structure of individual solvated nanocrystals,[16,17] yet probing the solution chemistry in these systems has remained a challenge. Radiolysis induced by the electron beam is thought to dominate the chemistry in LCTEM, is challenging to replicate *ex situ,* and chemical intuition from 'traditional' chemistry often does not hold during radiolysis. However, with careful experimental design, gold nanocrystals can be used as a chemical probe to elucidate the major reactive species present in LCTEM.

When a high energy electron beam irradiates an aqueous solution, it produces a variety of radiolytic products, including OH·, H_2O_2, and H·, among others.[18–20] Schneider, et. al developed a kinetic model to understand how the electron dose rate affects the concentrations of different radiolytic species.[21] They showed that by switching from a low dose rate to high dose rate regime, the liquid cell can be modulated from an oxidizing to a reducing environment, respectively, by altering the balance of highly oxidizing species (OH·) and highly reducing species (e^-_{aq}). Experimentally, it was shown that in the high dose rate regime, the etch rate of gold nanocrystals is directly dependent on the electron dose rate,[14] indicating a close relationship between gold nanocrystal etching and radiolytic products.

In typical graphene LCTEM etching experiments preformed previously in our group, the encapsulating solution contains HCl to control the stability of AuNCs[22] and prevent hydrolysis of added metal salts.[13–15] It is well known that the vast majority of hydroxyl radicals (>90%) are scavenged in the presence of halides to produce halide-based radicals.[23–31] When halides scavenge hydroxyl radicals, the major radical product is $X_2^{\cdot-}$, where X = Cl, Br, or I.[26] Furthermore, bromide and iodide are far more efficient radical scavengers than chloride, as the intermediate formed from the initial reaction between halides and hydroxyl radicals primarily reverts back to the initial state in the case of chloride. For bromide and iodide, this intermediate is stabilized and continues reacting to form $Br_2^{\cdot-}$ and $I_2^{\cdot-}$ radicals. Consequently, the concentration of bromide or iodide containing radicals in solution will be greater than chloride containing radicals, even with a 600-fold greater concentration of chloride ion present.[26] This means that even minute quantities of bromide or iodide present in the encapsulating solution of LCTEM can drastically alter the radiolytic environment.

One hypothesis is that the highly oxidizing hydroxyl radicals are responsible for etching gold nanocrystals in graphene LCTEM.[13–15,32] If this were the case, the etch rate would be modulated with chemical additives to alter the power of the oxidant. When halides scavenge hydroxyl radicals, the standard reduction potential is drastically reduced from OH· to $I_2^{\cdot-}$ ($E(OH\cdot/OH^-)$ = 2.73 V *vs.* $E(I_2^{\cdot-}/2I^-)$ = 1.05 V), indicating a marked decrease in the strength of the oxidant (Scheme 1, left). Accordingly, one would expect the average etch rate of the gold nanocrystals to *decrease* in the presence of heavier halides.

A second hypothesis for the role of halides in LCTEM etching studies is their possible function as complexation agents for oxidized gold ions, thus serving to stabilize the products of the oxidation. Addition of heavier halides to the system can lower the reduction potential of gold by *c.a.* 600 mV (Scheme 1, right). This would present itself as an *increase* in etch rate in the presence of heavier halides, opposite of the trend expected for the halides if their radical species are acting as the oxidizing agents for the gold nanocrystal. By observing the trend in etch rate of AuNCs as heavier halides are added, the dominating mechanism can be elucidated. Further, it is critical to understand the role of halides in LCTEM experiments, as halides are present as HCl in the encapsulating solution, or through an ionic surface ligand (i.e. cetyltrimethylammonium bromide (CTAB)). Additionally, as halides from halide-containing ligands such as CTAB would introduce minute quantities of halides, it is important to understand the role of sub-stoichiometric concentrations of halides in graphene LCTEM etching experiments of AuNCs. Though the effects of halides in LCTEM of AuNCs have been acknowledged,[22,33–35] the highly non-linear effects in halide mixtures warrant careful study to elucidate the relative role of complexation and radical chemistry to the observed etching trajectories.

While careful observation of nanocrystal etching trajectories in different chemical environments provides a route to understand the etching chemistry, it is unable to identify the key reactive chemical intermediates (*i.e.* radiolysis products)

Scheme 1. Radical chemistry *vs.* coordination chemistry hypotheses for the effect of halides on AuNC etching in LCTEM

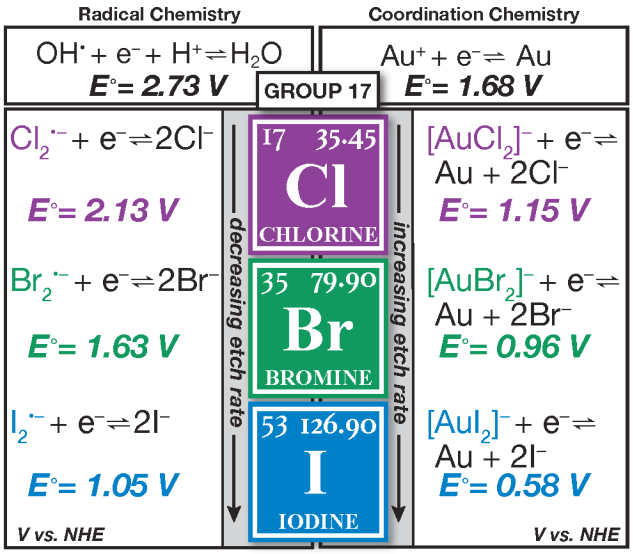

which are responsible for etching. Pulse radiolysis is a technique in which a high energy pulsed electron beam irradiates a solution of interest which is probed by time resolved optical spectroscopy. Through this technique, a solution can be irradiated with the same radiation source and at a peak dose rate that is approximately the same as the steady state dose rate of LCTEM ($4.25\times10^{9} Gy/s$ peak in pulse radiolysis *vs* $1.14\times10^{9} Gy/s$ steady state in graphene LCTEM). While the continuous irradiation in LCTEM provides much higher average power than in pulsed systems, the products formed in pulse radiolysis are likely still formed in LCTEM at short timescales. Accordingly, pulse radiolysis may provide a route to direct chemical identification of key reactive intermediates in graphene liquid cell (GLC) encapsulation solutions.

$FeCl_3$ is frequently introduced as the etchant for LCTEM etching experiments.[13–15,32,36] Previous reports hypothesized that Fe(III) is reduced by solvated electrons to Fe(II) which then catalytically produces sufficient hydroxyl radicals through a Fenton's type mechanism to etch gold.[14] While this mechanism is certainly one of the many simultaneously occurring reactions in a greater reaction network, the feasibility of this mechanism in LCTEM has not been investigated. An alternate possibility that, to date, has not been considered is that the preloaded Fe(III) complex is oxidized to a highly reactive species with sufficient potential to etch gold directly. Under the highly oxidizing conditions in LCTEM, it seems plausible that added metal complexes could be oxidized through a ligand/or the metal center itself.

In this work, we aim to unravel the role of halides and iron during oxidative etching of gold nanocrystals in graphene LCTEM. We achieve this by combining *in situ* microscopic studies using graphene LCTEM with *in situ* spectroscopic studies using pulse radiolysis, combined with radical reaction network models and quantum chemical calculations of possible key intermediate species. In this manner, we can elucidate the roles of certain additives to nanocrystal transformations in graphene LCTEM, while pulse radiolysis can provide insight into the identity of the species causing these transformations. We designed a series of graphene LCTEM experiments to track the etch rate of gold nanocrystals in the presence of chloride, bromide, and iodide to elucidate their effect on etch rate. The increase in etch rate as we add heavier halides indicates that the predominating role of halides in graphene LCTEM is to act as complexation agents, rather than the active oxidant. The lack of etching in all halide environments in the absence of $FeCl_3$ indicate that iron is significant in the mechanism of gold nanocrystal etching. Accordingly, pulse radiolysis measurements were performed on GLC solutions with and without $FeCl_3$ to gain a better sense of iron's role in the AuNC etching mechanism. The observed ground state bleaching of the Fe(III) absorption band suggests that the Fe(III) complex may be oxidized by radiolytically produced radicals. CASSCF calculations suggest that an oxidized iron complex with a OH ligand is likely the reactive form of iron in solution. Finally, we suggest a mechanism consistent with this data, where the radiolytically produced oxidized iron complex oxidizes the gold nanocrystal, while the halides control the rate of removal of the gold atoms.

METHODS

Nanoparticle Synthesis: Gold nanocrystals were synthesized following a modified procedure published previously[3].

Preparation of Seeds: Briefly, 10mL of 100mM cetyltrimethylammonium chloride (CTAC) and 0.25mL of 10mM hydrochloroauric acid ($HAuCl_4$) was added to a clean, 20mL vial. The vial was put into a water bath set to 30 °C and was stirred rapidly. 0.45 mL of 20 mM $NaBH_4$ was added, allowed to stir for 1 minute, then left undisturbed at 30 °C for 1.5 hr to decompose any excess $NaBH_4$.

Preparation of Nanocrystals: Two identical solutions of 9.5 mL of 100mM CTAC, 0.25 mL of 10 mM $HAuCl_4$, and 90 μL of 40 mM ascorbic acid (AA) were each added to clean 20 mL vials, in order. To the first vial, 25 μL of the seed solution was added during rapid stirring until the solution turned pale pink (approximately 5 s). Then, 300 μL of this solution was added into the other vial, briefly mixed and left to sit on the bench for 15 mins to allow the growth to complete. Then solution was then washed and resuspended in water three times by centrifugation at 8000 rpm for 10 minutes. After the final washing, the nanocrystals were concentrated to an OD of 1, then stored in a vial in the dark.

Graphene Liquid Cell (GLC) Preparation: Graphene liquid cells were prepared as described previously.[37] The encapsulating solutions were prepared as follows: 100 mM solution of $FeCl_3$ was prepared in

0.1 M HCl to prevent hydrolysis of the iron. 100 μL of the $FeCl_3$ solution and 100 μL of water were added to a small vial. 10 μL of the desired AuNC solution was added just before assembly of the GLC. For samples with Br^- or I^-, concentrated HBr or HI was serially diluted with Milli-Q water to a 0.8 mM concentration. 100 μL of this solution was added to a vial with 100 μL of the $FeCl_3$ in HCl as described above.

In-Situ TEM Imaging: All experiments were performed on a FEI Tecnai S-Twin T-20 TEM operating at 200 kV with a LaB_6 filament. *In situ* videos were collected with a Gatan Rio 16 IS camera using the Digital Micrograph *in situ* data collection function. Videos were binned by two for 2048 x 2048 resolution. The nominal magnification was 97 kx for a pixel resolution of 1.4 Å/pixel. The frame rate for most videos was 5 fps, yielding a temporal resolution of 0.2 s. The frame rate of videos containing iodide and no iron was 2 fps, yielding a temporal resolution of 0.5s. To convert CCD counts to electrons, a conversion value of 124 was used and all videos were taken at 800 $e^-/Å^2s$, except for the GLCs without iron, which were taken at 2000 $e^-/Å^2s$. It is important to note that there may be a slight inaccuracy in this conversion value, but as all videos were taken at the same dose rate, the conclusions of this paper are independent of its exact value. Additionally, this conversion value is different from that in previous publications from our group[14] since we have updated our camera system. So far, we have been unable to determine a conversion value from our previous camera to this one, so exact dose rates published in this and future works may be slightly different from previous publications.

Pulse Radiolysis: The pulse radiolysis experiments were carried out using 15 ns electron pulses from the 10 MeV linear accelerator ELEKTRONIKA-U003 (Toriy, Moscow). The dose delivered per pulse was measured by electron dosimetry and SCN dosimetry.[38] Doses of ~85 Gy/pulse were selected. The optical detection system consisted of a pulsed 1000 W xenon lamp (Osram, XBO1000), Suprasil cell (light path 1 cm), a high intensity grating monochromator (Acton research, SP500), an R928 photomultiplier (Hamamatsu Photonics) and a fast transient recorder (Tektronix, TDS5034B). Linac operation and data acquisition were done in the computer-controlled mode.

Theoretical Calculations: All calculations were carried out with the ORCA program package.[39] A revised B3LYP functional was employed for structure optimization which is optimized to estimate the energy splitting between different spin states.[40,41] The resolution of identity (RI) approximation was used to speed up Coulomb and exchange integrals.[42] All calculations employed the def2-TZVP basis set.[43] Dispersion forces were considered by an atom pairwise dispersion correction with the Becke-Johnson damping scheme[44,45] while solvation effects of water were incorporated by the Conductor-like Polarizable Continuum Model (C-PCM).[46] The structure was confirmed as a minimum on the potential energy surface by a semi numerical frequency calculation. Subsequently, CASSCF calculations were carried out. The final active space consists of 15 electrons in 10 orbitals for the initial complex and 14 electrons in 10 orbitals for the oxidized complex. The natural orbitals of the active space as well as a detailed discussion how the most stable isomer was identified can be found in the supporting information. Local spins were determined by the approach proposed by Herrmann, Reiher, and Hess.[47] All calculations were uploaded to the NOMAD repository with an embargo time of 3 months to support the FAIR data principles.

RESULTS AND DISCUSSION

Role of Halides

For the LCTEM studies, gold nanocrystals were specifically synthesized to contain minimal additives that affect the observed etch rate. The gold nanocrystals were synthesized in the absence of silver, and chloride containing CTAC ligands were used rather than bromide containing cetyltrimethylammonium bromide (CTAB), so that the concentration of bromide added to the encapsulating solution could be controlled. A concentrated solution of these pre-made spherical AuNCs were added to a solution of $FeCl_3$ and HCl to create the encapsulating solution. 40 mM $FeCl_3$ is added as the etchant precursor, while HCl is used to prevent hydrolysis of $FeCl_3$ and also tune the final Cl^- concentration to 190 mM. Enough HBr or HI was added to the respective solutions to bring the final concentration of Br^- or I^- to 0.38 mM. The amount of HX (where X= Br, I) added is low enough that the effect on pH is negligible. The exact role of $FeCl_3$ in graphene LCTEM is, to date, unknown, but a hypothesis is presented later in this report. $FeCl_3$ can etch gold in ambient conditions,[48] yet the rate of this is slow and the amount added in these experiments is low enough that minimal etching takes place before the *in situ* experiments begin. Once in the TEM, the beam is spread so that the dose rate imparted on the sample is very low (< 25 $e^-/Å^2s$). When a candidate particle is found, the beam is condensed using a home written script to a specified dose rate.[37] At this high dose rate, the combination of radiolysis species and $FeCl_3$ create a highly oxidizing environment in the liquid cell, where AuNC etching can be observed in real time.

Figure 1A shows a representative etching trajectory of a gold nanocrystal in chloride environment without iron, where Figure 1B shows the calculated projected area *vs.* time curve of the etching trajectory. This lack of etching was observed in all three halide environments without the presence of iron (see *Mov.* S1-3). Figure 1C, 1E, and 1G show

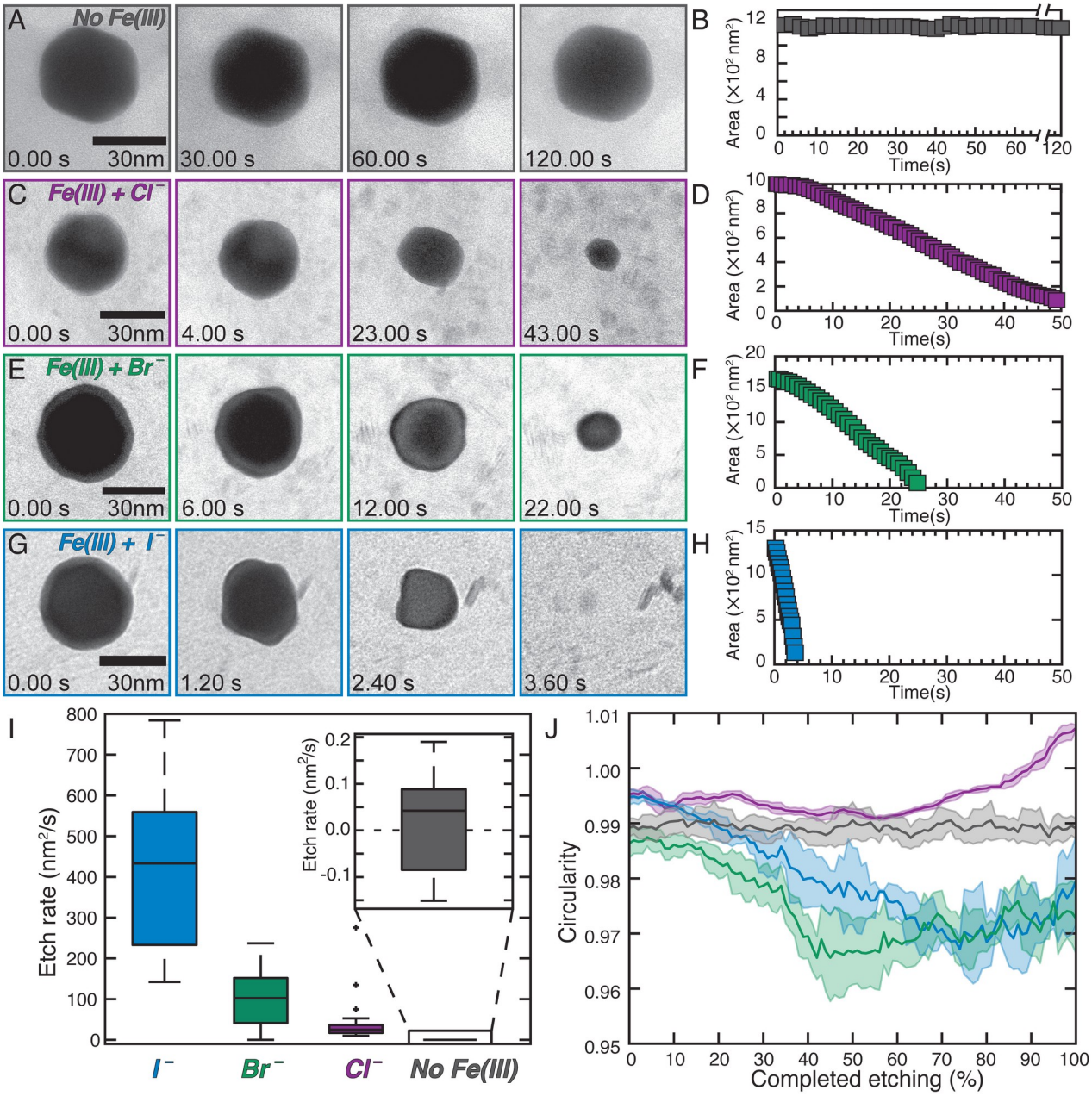

Figure 1. Effect of halides on oxidative etching of AuNCs. Etching trajectory and corresponding area *vs.* time curves for AuNCs in an aqueous encapsulating solution of 190mM $Cl^{-¿¿}$ (**A, B**), 40mM Fe(III) and 190mM $Cl^{-¿¿}$ (**C, D**), 40mM Fe(III), 190mM $Cl^{-¿¿}$, and 0.38mM $Br^{-¿¿}$ (**E, F**), and 40mM Fe(III), 190mM $Cl^{-¿¿}$, and 0.38mM $I^{-¿¿}$ (**G, H**). **I)** Box and whisker plot of the average AuNC etch rate in each conditions, totaling *ca.* 80 individual etching trajectories. Etch rates were determined by the slope of the area vs. time curves as shown in **B, D, F,** and **H**. The average is given by the line in the box, the interquartile range by the edges of the box, and the range of the rates is given by the whiskers. Outliers are marked with a cross. **J)** Circularity of the AuNC as it undergoes oxidative etching. A perfect circle has a circularity of C=1 while any deviations lead to C<1. The AuNC in solution with 190mM $Cl^{-¿¿}$ and 40mM Fe(III)(purple) maintains a constant circularity of ~C=1 while the AuNC in solution with 190mM $Cl^{-¿¿}$, 0.38mM $Br^{-¿¿}$ and 40mM Fe(III) (green) deviates from C=1 and is constantly changing throughout etching.

representative etching trajectories of gold nanocrystals in chloride, chloride and trace bromide, or chloride and trace iodide environments, respectively, all with $FeCl_3$ present. The calculated projected area *vs.* time curves of the etching trajectories of the gold nanocrystals in chloride, bromide, and iodide environments are shown in Figure 1D, 1F, and 1H, respectively.

Clearly, the etching time scale depends heavily on the species present in the GLC. Without any iron added, the nanocrystals do not etch measurably under the time scales studied. With Fe(III) added to the liquid cells, complete etching occurs in the case of all three halides (see *Mov.* S4-6). The rate of gold nanocrystal etching is modulated by the addition of different halides. The gold nanocrystals etch the fastest in the presence of iodide and the slowest in the presence of chloride. Figure 1I summarizes the etching rate of ~80 nanocrystals, as box and whisker plots, for each of the environments explored. From this plot, it is apparent that the etch rate increases going down group 17. This trend is consistent with halides acting as complexation agents for the gold ions, rather than active oxidants.

These results indicate that the halide dependent radical chemistry present in graphene LCTEM does not dominate the observed chemical transformations. Water-based and halide-based radicals are certainly formed once the liquid cell is exposed to the electron beam, but these radicals do not seem to drive the observed reaction trend. There are likely less radicals present in GLCs than is estimated through kinetic modeling, as graphene is known to scavenge radicals and create a milder environment.[49] This could decrease the concentration of halide radicals in the system, releasing halides to complex with gold ions. Ultimately, this allows 'traditional' chemical concepts to be studied at a single particle level with graphene LCTEM.

It is also evident that the interquartile range (*i.e.* the spread) of the etch rates in Figure 1I becomes larger in the case of large rates. One possibility is that as the etch rate increases, the exact rate becomes much more sensitive to the liquid cell geometry. For instance, if one liquid pocket is much thinner than another, then the etch rate will decrease due to a lower concentration of oxidizing species near the surface of the AuNC. While this same pocket-size variability is present in all cases, the slower etch rate allows more time for diffusion, potentially making it less sensitive to these differences.

Notably, the intermediate shapes of the nanocrystals as they undergo oxidative etching appear to become more anisotropic as heavier halides are added. Qualitatively, the AuNCs in solution with Cl^- maintains its spherical shape throughout etching, while the AuNCs in solution with Br^- and I^- become much more anisotropic. To quantify this, the circularity of the particle was calculated in each frame of the video (see Fig. S1 for details). Circularity (C) is a measure of how close a shape is to a perfect circle, where a perfect circle has C = 1, while anything that deviates from a circle will have C < 1. For reference, an n-sided polygon will increase in circularity as n increases, with C~0.9 for n=4.

Figure 1J demonstrates that the nanocrystals in solution with Cl^- maintains a constant circularity throughout the etching trajectory. In the case of added Br^- and I^-, the circularity begins near 1, but quickly decreases. Possible explanations for the decreased circularity when moving to heavier halides is two-fold. Bromide and iodide are well known to have strong affinity for certain gold facets,[50] while chloride does not. This affinity directs etching to certain facets,[7] decreasing the circularity of the gold nanocrystals. On the other hand, as the complexation energy increases when heavier halides are added, the overpotential for oxidative etching of gold also increases. The system with iodide present has over a 600 mV increase in overpotential compared to the system with just chloride. This increase likely moves the oxidative etching well into the diffusion limited regime, causing the oxidation to become anisotropic due to localized differences in the oxidative environment.

It is surprising that small concentrations of bromide and iodide can induce a significant increase in etch rate throughout the entire trajectory. If the AuNCs are oxidized to the Au(I) oxidation state, then two halides are needed to complex every gold atom. A gold nanocrystal 20 nm in diameter contains approximately 2×10^6 gold atoms, meaning that 4×10^6 halides need to be present in each liquid cell pocket to complex all the gold atoms. As the thickness of the GLCs are typically less than 200 nm,[11,51] the lateral dimension of the liquid cell needed to contain stoichiometric concentrations of

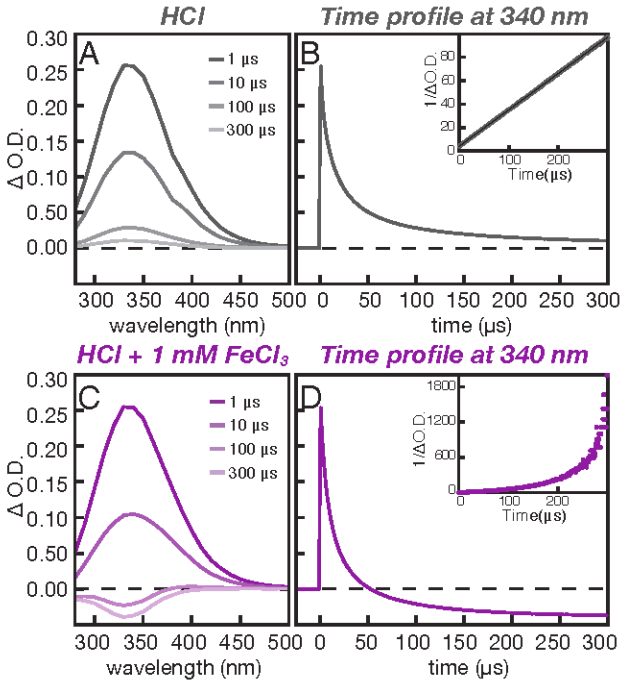

Figure 2. Pulse radiolysis measurement (85 Gy/pulse, 15 ns FWHM) of a 0.2 M HCl solution (**A, B**) and a 0.2 M HCl, 1 mM $FeCl_3$ solution (**C, D**) in N_2O saturated water. **A**) Transient absorption spectra of a 0.2 M HCl solution at 4 different times 1 µs, 10 µs, 100 µs, 300 µs. **B**) related time profile of the transient absorption decay at 340 nm. Inset: time profile at 340 nm plotted as 1/O.D. vs. time. The black line depicts a linear fit **C**) Transient absorption spectra of a 0.2 M HCl, 1 mM $FeCl_3$ solution at 4 different times 1 µs, 10 µs, 100 µs, 300 µs. **D**) Related time profile of the transient absorption decay at 340 nm. Inset: time profile at 340 nm plotted as 1/O.D. vs time. Note the O.D. values in the inset have been shifted by + 0.0378 to prevent the disruption due to the pole of the 1/x function for x=0.

bromide and iodide is on the order of 20 μm, far larger than the size of typical liquid cell pockets.[51,52] An excess of chloride is present in all the experiments, but if the complexation were to switch from a heavier halide to chloride in the middle of an etching trajectory, we would expect to see a distinct decrease in the etch rate due to the increasing reduction potential. This would manifest itself in the projected area *vs*. time curves as a decrease in etch rate as the etching trajectory progresses, or as a second linear portion of the graph with a smaller slope, which is not present in these etching trajectories.

To rationalize this, we must consider ways in which the trace halides may be recycled. This may indicate the presence of chemical loops inside the liquid cell pockets. In this manner, a single chemical species is repeatedly oxidized and reduced many times by radicals or other species present in the system. For instance, two halides from solution complex an oxidized gold atom on to form a $[AuX_2]^-$ complex. This complex could then be reduced by a solvated electron or hydrogen atom to form an Au^0 atom and two free X^- ions. These same halides are now available to complex another gold atom. This process constantly refreshes the supply of precursors to the system. In this case, even though there is a sub-stoichiometric concentration of bromide or iodide added to the system, the concentration of the heavy halide ion available to the system approaches a steady state, which would give rise to the constant etch rates observed in this study.

Role of Iron

In initial AuNC etching studies, iron in the form of $FeCl_3$ was empirically determined to be a suitable beam-initiated etchant precursor. However, the mechanism of etching remains unclear. Iron was previously proposed to be a catalyst to produce $^{\bullet}OH$ radicals through Fenton's mechanism,[14] as shown in equation (1).

$$Fe(II) + H_2O_2 \rightarrow Fe(III) + \cdot OH + OH^- \quad (1)$$

In the GLC, Fenton's reaction would occur as follows. Preloaded Fe(III) from $FeCl_3$ would be reduced by the electron beam to Fe(II). Fe(II) would then react with radiolytically produced H_2O_2 to catalytically produce $^{\bullet}OH$. Through this mechanism, the presence of iron would need to cause a significant increase in the concentration of $^{\bullet}OH$ to account for the significantly accelerated etch rate of AuNCs. Additionally, any hydroxyl radicals produced through this mechanism are likely to be scavenged by the halides, as discussed previously. Therefore, any additional hydroxyl radicals produced through Fenton's reaction would ultimately manifest as a greater concentration of the $X_2^{\bullet -}$ species, where X = Cl, Br, I. When Fenton's reaction is added to our kinetic model, we see no significant change in the concentration of hydroxyl radicals in the presence of halides, and even a slight decrease in ·OH concentration compared to when no iron is present (see Fig. S2). We have shown above that the gold nanocrystal etch rate increases with the presence of halides, moving down group 17. If the $X_2^{\bullet -}$ radicals were the active etchants in this system, the gold nanocrystal etch rate should decrease, even if the halides are acting as both complexation agents and oxidants (see Fig. S3). While Fenton's reaction is likely occurring to some extent in the liquid cell solution, it seems unlikely that this reaction accounts for the observed reactivity. It is well known that under the high electron dose rates used in this study, both highly reducing and oxidizing species are formed.[21] Under these conditions, it is possible that the preloaded Fe(III) is oxidized by radicals to some extent, and it is this oxidized iron complex that directly oxidizes the AuNC.

Pulse radiolysis was used to gain spectroscopic insight into the role of iron in graphene LCTEM experiments. Pulse radiolysis is a pump-probe technique that allows spectroscopic observation of the formation of short-lived radicals under electron radiation with nanosecond time resolution. Additionally, by using selective radical scavengers, it is possible to investigate the oxidative and reductive reaction pathways separately. In these experiments the solution of interest is placed into a flow cell system ensuring the desired gas saturation of the solution as well as allow for a renewal of the sample solution in the sample cell for every electron pulse. The sample is irradiated with an electron pulse with a peak dose rate of ~4.25 × 10^9 Gy/s (85 Gy / pulse and a 15 ns pulse width), comparable to the steady state dose rates used in graphene LCTEM. Using a fast-transient recorder, the absorption and decay of transient radical species can be observed within a 1 ms time domain. Herein, Δ O.D. is defined as the difference in optical density before (O.D. (GS), ground state absorption) and after (O.D.(T), transient) the electron pulse, as shown in equation (2).

$$\Delta O.D. = O.D.(T) - O.D.(GS) \quad (2)$$

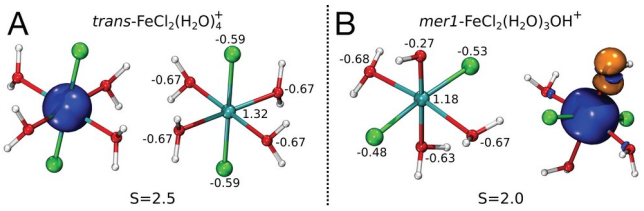

Figure 3. Mulliken partial charges and spin density isosurfaces from CASSCF calculations of **A**) *trans*-$FeCl_2(H_2O)_4^+$ and **B**) *mer1*-$FeCl_2(H_2O)_3OH^+$. See SI for information on active space. The blue isosurface highlights regions with increased alpha spin density while orange highlights regions of increased beta spin density.

Figure 2A and 2C depict the pulse radiolysis transient absorption spectra of an aqueous 0.2 M HCl solution and an aqueous 0.2 M HCl solution containing 1 mM $FeCl_3$, respectively, both saturated with N_2O. Such conditions lead to the production of three highly reactive species, namely $^{\bullet}H$, $^{\bullet}OH$, and e_{aq}^-, in addition to the molecular products H_2 and H_2O_2. Under our experimental conditions, N_2O is used to efficiently scavenge and convert e_{aq}^- into $^{\bullet}OH$. The $^{\bullet}OH$ radicals react with Cl^- and ultimately forms $Cl_2^{\bullet-}$ (see Table 1 for the detailed reaction cascade) which is discernable by the well-established transient absorption spectrum with a maximum at 340 nm.[53] This peak is observed in both pulse radiolysis transient absorption spectra with and without $FeCl_3$ (Fig. 2A and 2C). A first indication towards a potential reaction of $Cl_2^{\bullet-}$ with Fe(III) comes from the comparison of the transient spectra in the 100 µs range. When $FeCl_3$ is present, the decay of the $Cl_2^{\bullet-}$ transient absorption goes below zero in the UV part of the optical spectrum around 290-360 nm, where Fe(III) complexes show strong ground state absorption (see Fig. S4). This ground state bleaching indicates that less Fe(III) is present at this time than before the electron pulse, suggesting a potential reaction between Fe(III) and $Cl_2^{\bullet-}$. A similar behavior was also observed when probing the reaction of Fe(III) with $SO_4^{\bullet-}$, which is an even stronger oxidizing intermediate compared to $Cl_2^{\bullet-}$ (see Fig. S5 for details), indicating the Fe(III) may in general react with very strong oxidizing intermediates.

Table 1. Proposed reaction cascade in pulse radiolysis experiments

	$H_2O \rightsquigarrow e^-_{aq} + {}^{\bullet}H + {}^{\bullet}OH$
a)[54]	$N_2O + e^-_{aq} + H_2O \rightarrow N_2 + {}^{\bullet}OH + OH^-$
b)[54]	${}^{\bullet}OH + H^+ + Cl^- \rightarrow Cl{}^{\bullet} + H_2O$
c)[30]	$Cl{}^{\bullet} + Cl^- \rightarrow Cl_2^{\bullet-}$
d)[30]	$2Cl_2^{\bullet-} \rightarrow 2Cl^- + Cl_2$
e)	$2Cl_2^{\bullet-} + [Fe(III)L]^{x+} \rightarrow 2Cl^- + [Fe(ox)L]^{(x+1)+}$
f)	$2Cl_{(x+1)+}^{\bullet-} + [Fe(III)L]^{x+} \rightarrow 2\ Cl^- + [Fe(III)L(ox)]$

Further, the $Cl_2^{\bullet-}$ decay, as depicted by the 340 nm time absorption profile in Figures 2B and 2D can be evaluated to determine the kinetics of the reaction. Without any other potential reaction partners $Cl_2^{\bullet-}$ recombines in a disproportionation reaction (Table 1d). As expected for such a bimolecular recombination reaction when plotting 1/ΔO.D. *vs*. time for the 340 nm time profile (Fig. 2B, inset) in the systems without $FeCl_3$ the resulting graph can be

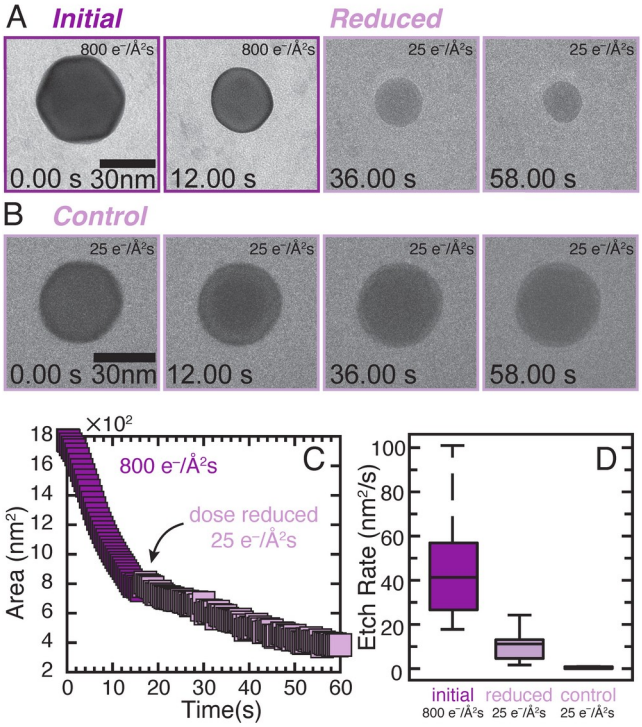

Figure 4. A) Etching trajectory of a AuNC in 40 mM Fe(III) and 190 mM Cl. The etching trajectories began at 800 e^-/ Å^{2}s but were reduced to 25 e^-/ Å^{2}s in the middle of etching. After the dose rate decrease, the nanocrystal continues etching. **B**) Control experiment showing that when the AuNC is initially irradiated at 25 e^-/ Å^{2}s the nanocrystal does not etch. **C**) Area *vs* time curve of the etching trajectory shown in **A**. The nanocrystal etches at a constant rate initially, consistent with the previous experiments. When the dose rate is decreased, the etch rate immediately slows, but etching continues. **D**) Box and whisker plots summarizing 19 different etching trajectories recorded under these conditions. The average etch rate of the AuNC after reducing the dose rate is significantly lower than the initial etch rate, but it is non-zero.

fitted linearly and from the slope a bimolecular recombination rate constant of $2k = 2.7 \times 10^9$ $M^{-1}s^{-1}$ was derived as the recombination rate constant for $Cl_2^{\bullet-}$ under our reaction conditions. Plotting 1/ΔO.D. *vs* time for the time profile of $Cl_2^{\bullet-}$ decay in the presence of Fe(III) (Fig. 2D, inset) shows a significant deviation from a linear relation, indicating a more complex reaction other than only the recombination of $Cl_2^{\bullet-}$. This further supports our hypothesis that the $Cl_2^{\bullet-}$ radical is reacting with Fe(III). Unfortunately, even if evidence for a reaction of $Cl_2^{\bullet-}$ with Fe(III) were obtained, the reaction of $Cl_2^{\bullet-}$ with Fe(III) is a minor channel and we have not been successful in obtaining a reliable rate constant for this reaction.

To consider how a reaction between Fe(III) and $Cl_2^{\bullet-}$ might be possible, we consider two pathways for the oxidation. $Cl_2^{\bullet-}$ can react with Fe(III) to oxidize the iron center ($[Fe(ox)L]^{x+}$) or the ligands ($[Fe(III)L(ox)]^{x+}$). To explore the oxidation of the ligands, we first consider the ligand shell present on the iron ion. At the chloride concentration used in these studies, there is likely 1-2 Cl^- ligands present in the iron(III)-aqua complex.[55] All possible isomers with 1-2 Cl^- ligands were investigated through DFT calculations to determine the most stable structure (see SI for more details). Under these experimental conditions, the *trans*-$[FeCl_2(H_2O)_4]^+$ structure (Fig. 3A) was found to be most stable in solution. Upon oxidation, the *trans*-$[FeCl_2(H_2O)_4]^+$ complex loses a H atom to become *mer1*-$[FeCl_2(H_2O)_3OH^+]$. CASSCF (14,10) calculations were used subsequently to determine the electronic structure of the oxidized complex. Figure 3B shows the isosurface of the spin density indicating that the OH ligand plays an important role in the electronic structure of the complex. This is supported by a local spin analysis revealing a complex which resembles a high-spin Fe(IV) complex ($<S_Z>$=2.14) antiferromagnetic coupled to the OH-ligand ($<S_Z>$=-0.14). Additionally, comparison of the Mulliken partial charge of *mer1*-$[FeCl_2(H_2O)_3OH^+]$ to *trans*-$[FeCl_2(H_2O)_4]^+$ indicates that it is mainly the O atom of the OH ligand that is oxidized, while the electron density around the iron center is slightly increased. This suggests that the role of iron in the LCTEM experiments may be to stabilize the reactive radical species by complexing to the iron center. Considering the pulse radiolysis data, it seems plausible that the $Cl_2^{\bullet-}$ radical oxidizes the Fe(III) complex in solution to decay into its products. The oxidized iron complex then stabilizes itself by donating a hydrogen atom to form *mer1*-$[FeCl_2(H_2O)_3OH^+]$, supported by the high acidity of the unprotonated complex. Then the oxidized hydroxyl ligand bound to the iron center is the reactive species that oxidizes the gold nanocrystals.

The pulse radiolysis experiments suggest that the active iron species in our solution have extended lifetimes compared to radiolytically produced radical species. If the active iron species is long-lived, it may be possible to build up a concentration during electron beam irradiation that, upon removal of the electron beam, would continue to etch the gold nanocrystal. Figure 3A shows an etching trajectory of a gold nanocrystal in the same chloride solution as in Figure 1A. Halfway through the etching trajectory, the dose was decreased from 800 e^-/ Å^{2}s to 25 e^-/ Å^{2}s. The nanocrystal continued etching after removal of the high intensity beam, but at a slower etch rate (see *Mov.* S7). This is in contrast to constant irradiation at 25 e^-/ Å^{2}s without the initial high dose period, which leads to negligible etching (Fig. 4B). We

confirmed that the nanocrystals were in liquid rather than in a dry pocket (see Fig. S6) in these control experiments. Figure 4C shows a representative area vs. time curve for the nanocrystals originally irradiated at a high dose rate. Etching of the nanocrystals continues after the dose is decreased, albeit at a much slower rate. This indicates that a concentration of a long-lived oxidant is built up during the high dose rate regime. Then, once the dose rate is decreased, the excess oxidant in solution can diffuse to the surface of the nanocrystal and continue oxidatively etching the gold. Figure 4D shows this data for several different etching trajectories, presenting the reproducibility of this trend.

The lifetime of the $Cl_2^{\bullet-}$ radical in this system is on the order of a few hundred microseconds (Figure 2B), while water-based radicals have much shorter lifetimes. Based on this, any radicals formed while the liquid cell was irradiated with a high dose rate should decay less than 1 ms after the dose is de- creased. The prolonged etching after the dose rate is decreased indicates it is unlikely that a water or halide-based radical is responsible for gold nanocrystal etching. This experiment supports the pulse radiolysis data indicating the formation of a long-lived transient species that is directly involved in the gold nanocrystal etching.

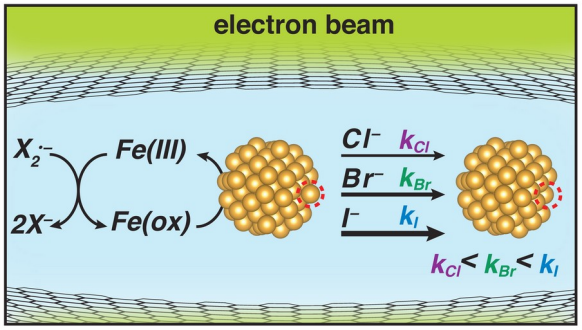

Figure 5. Proposed mechanism of AuNC etching in graphene LCTEM.

Taking into account the role of the halides and the role of the iron species in graphene LCTEM, we propose a mechanism consistent with the data, as shown in Figure 5. First, radiolysis induced by the electron beam creates a significant concentration of oxidizing radicals. These radicals react with the preloaded Fe(III) to form an oxidized iron transient species. The oxidized iron transient species then oxidizes the gold nanocrystal. Yet the rate at which the gold nanocrystal is oxidized is controlled by the type of halide present. The standard reduction potential for gold decreases in the presence of heavier halides, effectively increasing the overpotential and increasing the rate of oxidation.

CONCLUSION

Understanding the chemical processes occurring in LCTEM is crucial to determine the mechanism of nanocrystal etching. We have shown that introducing trace amounts of halides can significantly modulate the etch rate of gold nanocrystals under electron beam irradiation. While the halides are also known to create oxidizing radical species, in this system their dominating role is as a complexation agent for the oxidized gold ions. Yet it is possible that the halide radicals may play a much bigger role when studying less-stable systems, such as semiconducting or metal oxide nanocrystals, or when imaging in a SiN liquid cell as any radical scavenging effect from the graphene is absent. It is important to consider the effect of halides, even in minute quantities, as low concentrations in solution can cause significant effects under electron-beam irradiation.

A distinct lack of etching of gold nanocrystals in the absence of preloaded $FeCl_3$ indicates that iron plays a significant role in the etching mechanism. A combination of LCTEM experiments, pulse radiolysis experiments, and theoretical calculations suggest that the added iron (III) species is oxidized by radicals, into a highly reactive yet long lived, oxidized complex. This complex is responsible for the etching of gold nanocrystals in LCTEM, contrary to previous reports proposing $^{\bullet}OH$ radicals as the active oxidant. Further, it is possible that this behavior is not limited to iron salts and indicates that care must be taken to consider the reactivity of metal ions which may be present in the solution or in the material of interest during liquid cell observation. This study points to the importance of understanding the additives in the encapsulating solution. Ultimately, this is a step towards defining the chemical environment within graphene LCTEM to aid in better control and interpretation of LCTEM experiments.

ASSOCIATED CONTENT

Supporting Information

The Supporting Information is available free of charge on the ACS Publications website.

Movie S1. AuNC in 190 mM Cl^-, no Fe (AVI)
Movie S2. AuNC in 190 mM Cl^-, 0.38 mM Br^-, no Fe (AVI)
Movie S3. AuNC in 190 mM Cl^-, 0.38 mM I^-, no Fe (AVI)
Movie S4. AuNC etching in 190 mM Cl^-, 40 mM Fe(III) (AVI)
Movie S5. AuNC etching in 190 mM Cl^-, 0.38 mM Br^-, 40 mM Fe(III) (AVI)
Movie S6. AuNC etching in 190 mM Cl^-, 0.38 mM I^-, 40 mM Fe(III) (AVI)
Movie S7. AuNC etching in 190 mM Cl^-, 40 mM Fe(III), dose decrease from 800 to 25 $e^-/Å^2s$ (AVI)

Circularity calculation, presence of liquid in 25 $e^-/Å^2$s controls, *in situ* UV-Vis study of halides, kinetic modeling of [•OH] in different halide environments, AuNC etching overpotentials with halide radicals as oxidants, absorption spectrum of ground state $FeCl_3$ solution, pulse radiolysis studies with $K_2S_2O_8$, table of reactions used in kinetic model, details of DFT and CASSCF calculations

AUTHOR INFORMATION

Corresponding Author

* paul.alivisatos@berkeley.edu

Present Addresses

^ Currently at Leibniz Institute of Surface Engineering (IOM), Permoserstr. 15, D-04318 Leipzig, Germany

Author Contributions

The manuscript was written through contributions of all authors. All authors have given approval to the final version of the manuscript.

Funding Sources

The work was supported by the U.S. Department of Energy, Office of Science, Office of Basic Energy Sciences, Materials Sciences and Engineering Division under contract no. DE- AC02-05-CH11231 within the Physical Chemistry of Inorganic Nanostructures Program (KC3103).

Notes

The authors declare no competing financial interest

ACKNOWLEDGMENT

The LCTEM experiments were supported by the U.S. Department of Energy, Office of Science, Office of Basic Energy Sciences, Materials Sciences and Engineering Division, under Contract No. DE-AC02-05-CH11231 within the Physical Chemistry of Inorganic Nanostructures Program (KC3103). M.F.C. gratefully acknowledges support from the National Science Foundation's Graduate Research Fellowship Program (NSF GRFP). J.C.O gratefully acknowledges the support of the Kavli Philomathia Graduate Student Fellowship. Computational time from ZIH-Dresden is gratefully acknowledged. The authors would also like to acknowledge Negest Williams for her valuable administrative support.

REFERENCES

(1) Tran, M.; DePenning, R.; Turner, M.; Padalkar, S. Effect of Citrate Ratio and Temperature on Gold Nanoparticle Size and Morphology. *Mater. Res. Express* **2016**, *3* (10), 105027. https://doi.org/10.1088/2053-1591/3/10/105027.

(2) Nikoobakht, B.; El-Sayed, M. A. Preparation and Growth Mechanism of Gold Nanorods (NRs) Using Seed-Mediated Growth Method. *Chem. Mater.* **2003**, *15* (10), 1957–1962. https://doi.org/10.1021/cm020732l.

(3) Wu, H.-L.; Kuo, C.-H.; Huang, M. H. Seed-Mediated Synthesis of Gold Nanocrystals with Systematic Shape Evolution from Cubic to Trisoctahedral and Rhombic Dodecahedral Structures. *Langmuir* **2010**, *26* (14), 12307–12313. https://doi.org/10.1021/la1015065.

(4) Leff, D. V.; Ohara, P. C.; Heath, J. R.; Gelbart, W. M. Thermodynamic Control of Gold Nanocrystal Size: Experiment and Theory. *J. Phys. Chem.* **1995**, *99* (18), 7036–7041. https://doi.org/10.1021/j100018a041.

(5) Smith, D. K.; Miller, N. R.; Korgel, B. A. Iodide in CTAB Prevents Gold Nanorod Formation. *Langmuir* **2009**, *25* (16), 9518–9524. https://doi.org/10.1021/la900757s.

(6) Rayavarapu, R. G.; Ungureanu, C.; Krystek, P.; Van Leeuwen, T. G.; Manohar, S.; Materials, M. Iodide Impurities in Hexadecyltrimethylammonium Bromide (CTAB) Products: Lot-Lot Variations and Influence on Gold Nanorod Synthesis. *Langmuir* **2010**, *26* (7), 5050–5055. https://doi.org/10.1021/la100166f.

(7) Langille, M. R.; Personick, M. L.; Zhang, J.; Mirkin, C. A. Defining Rules for the Shape Evolution of Gold Nanoparticles. *J. Am. Chem. Soc.* **2012**, *134* (35), 14542–14554. https://doi.org/10.1021/ja305245g.

(8) O'Brien, M. N.; Jones, M. R.; Brown, K. A.; Mirkin, C. A. Universal Noble Metal Nanoparticle Seeds Realized Through Iterative Reductive Growth and Oxidative Dissolution Reactions. *J. Am. Chem. Soc.* **2014**, *136* (21), 7603–7606. https://doi.org/10.1021/ja503509k.

(9) Niu, W.; Zheng, S.; Wang, D.; Liu, X.; Li, H.; Han, S.; Chen, J.; Tang, Z.; Xu, G. Selective Synthesis of Single-Crystalline Rhombic Dodecahedral, Octahedral, and Cubic Gold Nanocrystals. *J. Am. Chem. Soc.* **2009**, *131* (2), 697–703. https://doi.org/10.1021/ja804115r.

(10) Zheng, H.; Smith, R. K.; Jun, Y. -w.; Kisielowski, C.; Dahmen, U.; Alivisatos, A. P. Observation of Single Colloidal Platinum Nanocrystal Growth Trajectories. *Science* **2009**, *324* (5932), 1309–1312. https://doi.org/10.1126/science.1172104.

(11) Yuk, J. M.; Crommie, M. F.; Zettl, A.; Alivisatos, A. P. High Resolution EM of Colloidal Nanocrystal Growth Using Graphene Liquid Cells. *Science* **2012**, *336*. https://doi.org/10.1126/science.1218693.

(12) Wang, Y.; Peng, X.; Abelson, A.; Xiao, P.; Qian, C.; Yu, L.; Ophus, C.; Ercius, P.; Wang, L. W.; Law, M.; et al. Dynamic Deformability of Individual PbSe Nanocrystals during Superlattice Phase Transitions. *Sci. Adv.* **2019**, *5* (6). https://doi.org/10.1126/sciadv.aaw5623.

(13) Ye, X.; Jones, M. R.; Frechette, L. B.; Chen, Q.; Powers, A. S.; Ercius, P.; Dunn, G.; Rotskoff, G. M.; Nguyen, S. C.; Adiga, V. P.; et al. Single-Particle Mapping of Nonequilibrium Nanocrystal Transformations. *Science* **2016**, *354* (6314), 874–877. https://doi.org/10.1126/science.aah4434.

(14) Hauwiller, M. R.; Ondry, J. C.; Chan, C. M.; Khandekar, P.; Yu, J.; Alivisatos, A. P. Gold Nanocrystal Etching as a Means of Probing the Dynamic Chemical Environment in Graphene Liquid Cell Electron Microscopy. *J. Am. Chem. Soc.* **2019**, *141* (10), 4428–4437. https://doi.org/10.1021/jacs.9b00082.

(15) Hauwiller, M. R.; Frechette, L. B.; Jones, M. R.; Ondry, J. C.; Rotskoff, G. M.; Geissler, P.; Alivisatos, A. P. Unraveling Kinetically-Driven Mechanisms of Gold Nanocrystal Shape Transformations Using Graphene Liquid Cell Electron Microscopy. *Nano Lett.* **2018**, *18* (9), 5731–5737. https://doi.org/10.1021/acs.nanolett.8b02337.

(16) Park, J.; Zettl, A.; Alivisatos, A. P. 3D Structure of Individual Nanocrystals in Solution by Electron Microscopy. *Science* **2015**, *349* (6245), 287–290. https://doi.org/10.1126/science.aaa7974.

(17) Kim, B. H.; Heo, J.; Kim, S.; Reboul, C. F.; Chun, H.; Kang, D.; Bae, H.; Hyun, H.; Lim, J.; Lee, H.; et al. Critical Differences in 3D Atomic Structure of Individual Ligand-Protected Nanocrystals in Solution. *Science* **2020**, *368* (6486), 60–67. https://doi.org/10.1126/science.aax3233.

(18) Draganić, I. G.; Draganić, Z. D. The Radiation Chemistry of Water; Academic Press, INC.: New York and

London, 1971. https://doi.org/10.1016/B978-0-12-221650-3.50006-6.

(19) Allen, A. *The Radiation Chemistry of Water and Aqueous Solutions.*; Van Nostrand: Princeton N.J., 1961.

(20) Schwarz, H. A. Applications of the Spur Diffusion Model to the Radiation Chemistry of Aqueous Solutions. *J. Phys. Chem.* **1969**, *73* (6), 1928–1937. https://doi.org/10.1021/j100726a047.

(21) Schneider, N. M.; Norton, M. M.; Mendel, B. J.; Grogan, J. M.; Ross, F. M.; Bau, H. H. Electron–Water Interactions and Implications for Liquid Cell Electron Microscopy. *J. Phys. Chem. C* **2014**, *118* (38), 22373–22382. https://doi.org/10.1021/jp507400n.

(22) Hermannsdörfer, J.; de Jonge, N.; Verch, A. Electron Beam Induced Chemistry of Gold Nanoparticles in Saline Solution. *Chem. Commun.* **2015**, *51* (91), 16393–16396. https://doi.org/10.1039/C5CC06812F.

(23) Mopper, K.; Zhout, X. Hydroxyl Radical Photoproduction in the Sea and Its Potential Impact on Marine Processes. *Science* **1990**, *250* (4981), 661–664.

(24) Zhou, X.; Mopper, K. Determination of Photochemically Produced Hydroxyl Radicals in Seawater and Freshwater. *Mar. Chem.* **1990**, *30* (C), 71–88. https://doi.org/10.1016/0304-4203(90)90062-H.

(25) Hata, K.; Inoue, H.; Kojima, T.; Iwase, A.; Kasahara, S.; Hanawa, S.; Ueno, F.; Tsukada, T. Hydrogen Peroxide Production by Gamma Radiolysis of Sodium Chloride Solutions Containing a Small Amount of Bromide Ion. *Nucl. Technol.* **2016**, *193* (3), 434–443. https://doi.org/10.13182/NT15-32.

(26) Zhang, K.; Parker, K. M. Halogen Radical Oxidants in Natural and Engineered Aquatic Systems. *Environ. Sci. Technol.* **2018**, *52* (17), 9579–9594. https://doi.org/10.1021/acs.est.8b02219.

(27) Rafi, A.; Sutton, H. C. Radiolysis of Aerated Solutions of Potassium Bromide. *Trans. Faraday Soc.* **1965**, *61*, 877. https://doi.org/10.1039/tf9656100877.

(28) Ward, J. F.; Myers, L. S. The Effect of Chloride Ions on Some Radiation Chemical Reactions in Aqueous Solution. *Radiat. Res.* **1965**, *26* (4), 483. https://doi.org/10.2307/3571859.

(29) Atinault, E.; De Waele, V.; Schmidhammer, U.; Fattahi, M.; Mostafavi, M. Scavenging of Es- and OH{radical Dot} Radicals in Concentrated HCl and NaCl Aqueous Solutions. *Chem. Phys. Lett.* **2008**, *460* (4–6), 461–465. https://doi.org/10.1016/j.cplett.2008.06.048.

(30) Jayson, G. G.; Parsons, B. J.; Swallow, A. J. Some Simple, Highly Reactive, Inorganic Chlorine Derivatives in Aqueous Solution. Their Formation Using Pulses of Radiation and Their Role in the Mechanism of the Fricke Dosimeter. *J. Chem. Soc. Faraday Trans. 1 Phys. Chem. Condens. Phases* **1973**, *69*, 1597. https://doi.org/10.1039/f19736901597.

(31) Parker, K. M.; Mitch, W. A. Halogen Radicals Contribute to Photooxidation in Coastal and Estuarine Waters. *Proc. Natl. Acad. Sci.* **2016**, *113* (21), 5868–5873. https://doi.org/10.1073/pnas.1602595113.

(32) Chen, L.; Leonardi, A.; Chen, J.; Cao, M.; Li, N.; Su, D.; Zhang, Q.; Engel, M.; Ye, X. Imaging the Kinetics of Anisotropic Dissolution of Bimetallic Core–Shell Nanocubes Using Graphene Liquid Cells. *Nat. Commun.* **2020**, *11* (1), 1–10. https://doi.org/10.1038/s41467-020-16645-3.

(33) Park, J. H.; Schneider, N. M.; Grogan, J. M.; Reuter, M. C.; Bau, H. H.; Kodambaka, S.; Ross, F. M. Control of Electron Beam-Induced Au Nanocrystal Growth Kinetics through Solution Chemistry. *Nano Lett.* **2015**, *15* (8), 5314–5320. https://doi.org/10.1021/acs.nanolett.5b01677.

(34) Woehl, T. J.; Abellan, P. Defining the Radiation Chemistry during Liquid Cell Electron Microscopy to Enable Visualization of Nanomaterial Growth and Degradation Dynamics. *J. Microsc.* **2017**, *265* (2), 135–147. https://doi.org/10.1111/jmi.12508.

(35) Chee, S. W.; Pratt, S. H.; Hattar, K.; Duquette, D.; Ross, F. M.; Hull, R. Studying Localized Corrosion Using Liquid Cell Transmission Electron Microscopy. *Chem. Commun.* **2015**, *51* (1), 168–171. https://doi.org/10.1039/c4cc06443g.

(36) Jiang, Y.; Zhu, G.; Dong, G.; Lin, F.; Zhang, H.; Yuan, J.; Zhang, Z.; Jin, C. Probing the Oxidative Etching Induced Dissolution of Palladium Nanocrystals in Solution by Liquid Cell Transmission Electron Microscopy. *Micron* **2017**, *97*, 22–28. https://doi.org/10.1016/j.micron.2017.03.003.

(37) Hauwiller, M. R.; Ondry, J. C.; Alivisatos, A. P. Using Graphene Liquid Cell Transmission Electron Microscopy to Study in Situ Nanocrystal Etching. *J. Vis. Exp.* **2018**, No. 135, 57665. https://doi.org/10.3791/57665.

(38) Fielden, E. M. Chemical Dosimetry of Pulsed Electron and X-Ray Sources in the 1-20 MeV Range. In *The Study of Fast Processes and Transient Species by Electron Pulse Radiolysis*; 1981; Vol. 86, pp 49–61.

(39) Neese, F. The ORCA Program System. *Wiley Interdiscip. Rev. Comput. Mol. Sci.* **2012**, *2* (1), 73–78. https://doi.org/10.1002/wcms.81.

(40) Reiher, M.; Salomon, O.; Hess, B. A. Reparameterization of Hybrid Functionals Based on Energy Differences of States of Different Multiplicity. *Theor. Chem. Acc.* **2001**, *107* (1), 48–55. https://doi.org/10.1007/s00214-001-0300-3.

(41) Kepp, K. P. Theoretical Study of Spin Crossover in 30 Iron Complexes. *Inorg. Chem.* **2016**, *55* (6), 2717–2727. https://doi.org/10.1021/acs.inorgchem.5b02371.

(42) Weigend, F. Hartree–Fock Exchange Fitting Basis Sets for H to Rn. *J. Comput. Chem.* **2006**, *29*, 167–175. https://doi.org/10.1002/jcc.

(43) Weigend, F.; Ahlrichs, R. Balanced Basis Sets of Split Valence, Triple Zeta Valence and Quadruple Zeta Valence Quality for H to Rn: Design and Assessment of Accuracy. *Phys. Chem. Chem. Phys.* **2005**, *7* (18), 3297–3305. https://doi.org/10.1039/b508541a.

(44) Grimme, S.; Antony, J.; Ehrlich, S.; Krieg, H. A Consistent and Accurate Ab Initio Parametrization of Density Functional Dispersion Correction (DFT-D) for the 94 Elements H-Pu. *J. Chem. Phys.* **2010**, *132* (15). https://doi.org/10.1063/1.3382344.

(45) Grimme, S.; Ehrlich, S.; Goerick, L. Effect of the Damping Function in Dispersion Corrected Density Functional Theory. *J. Comput. Chem.* **2011**, *32*, 1456–1465. https://doi.org/10.1002/jcc.

(46) Barone, V.; Cossi, M.; Tomasi, J. Geometry Optimization of Molecular Structures in Solution by the Polarizable Continuum Model. *J. Comput. Chem.* **1998**, *19* (4), 404–417. https://doi.org/10.1002/(SICI)1096-987X(199803)19:4<404::AID-JCC3>3.0.CO;2-W.

(47) Herrmann, C.; Reiher, M.; Hess, B. A. Comparative Analysis of Local Spin Definitions. *J. Chem. Phys.* **2005**, *122* (3). https://doi.org/10.1063/1.1829050.

(48) Zou, R.; Guo, X.; Yang, J.; Li, D.; Peng, F.; Zhang, L.; Wang, H.; Yu, H. Selective Etching of Gold Nanorods by Ferric Chloride at Room Temperature. *CrystEngComm* **2009**, *11* (12), 2797. https://doi.org/10.1039/b911902g.

(49) Cho, H.; Jones, M. R.; Nguyen, S. C.; Hauwiller, M. R.; Zettl, A.; Alivisatos, A. P. The Use of Graphene and Its Derivatives for Liquid-Phase Transmission Electron Microscopy of Radiation-Sensitive Specimens. *Nano Lett.* **2017**, *17* (1), 414–420. https://doi.org/10.1021/acs.nanolett.6b04383.

(50) Meena, S. K.; Celiksoy, S.; Schäfer, P.; Henkel, A.; Sönnichsen, C.; Sulpizi, M. The Role of Halide Ions in the Anisotropic Growth of Gold Nanoparticles: A Microscopic, Atomistic Perspective. *Phys. Chem. Chem. Phys.* **2016**, *18* (19), 13246–13254. https://doi.org/10.1039/C6CP01076H.

(51) Chen, Q.; Smith, J. M.; Park, J.; Kim, K.; Ho, D.; Rasool, H. I.; Zettl, A.; Alivisatos, A. P. 3D Motion of DNA-Au

Nanoconjugates in Graphene Liquid Cell Electron Microscopy. **2013**. https://doi.org/10.1021/nl402694n.

(52) Sasaki, Y.; Kitaura, R.; Yuk, J. M.; Zettl, A.; Shinohara, H. Efficient Preparation of Graphene Liquid Cell Utilizing Direct Transfer with Large-Area Well-Stitched Graphene. *Chem. Phys. Lett.* **2016**, *650*, 107–112. https://doi.org/10.1016/j.cplett.2016.02.066.

(53) Anbar, M.; Thomas, J. K. Pulse Radiolysis Studies of Aqueous Sodium Chloride Solutions 1. *J. Phys. Chem.* **1964**, *68* (12), 3829–3835. https://doi.org/10.1021/j100794a050.

(54) Buxton, G. V. Basic Radiation Chemistry of Liquid Water. In *The Study of Fast Processes and Transient Species by Electron Pulse Radiolysis*; 1982; pp 241–266.

(55) Persson, I. Ferric Chloride Complexes in Aqueous Solution: An EXAFS Study. *J. Solution Chem.* **2018**, *47* (5), 797–805. https://doi.org/10.1007/s10953-018-0756-6.

Insert Table of Contents artwork here